Electronic Supplementary Information

Parallel water photo-oxidation reaction pathways in hematite photoanodes: Implications for solar fuel production

Anton Tsyganok[1], Paulino Monroy-Castillero[2⁑], Yifat Piekner[1], Arik Yochelis[2,3*], Avner Rothschild[1,4**]

[1]*Department of Materials Science and Engineering, Technion - Israel Institute of Technology, Haifa 3200002, Israel*

[2]*Department of Solar Energy and Environmental Physics, Blaustein Institutes for Desert Research, Ben-Gurion University of the Negev, Sede Boqer Campus, Midreshet Ben-Gurion 8499000, Israel*

[3]*Department of Physics, Ben-Gurion University of the Negev, Be'er Sheva 8410501, Israel*

[4]*The Nancy & Stephen Grand Technion Energy Program (GTEP), Technion – Israel Institute of Technology, Haifa 3200002, Israel.*

[*]Correspondence: yochelis@bgu.ac.il

[**]Correspondence: avnerrot@technion.ac.il

⁑ Current address: General Coordination of Government Innovation, Government of Jalisco, Ciudad Creativa Digital, Guadalajara 44100, Mexico

S1. The dark current of the photoanode presented in the article

Figure S1 shows a cyclic voltammogram (CV) measured in dark, for the heteroepitaxial Zn-doped hematite photoanode presented in the article. The CV shows negligible dark current, in the ~20 nA/cm^2 range, through the whole potential range examined. This result indicates that the surface intermediates discussed in the article do not form without illumination that generates electrons and holes.

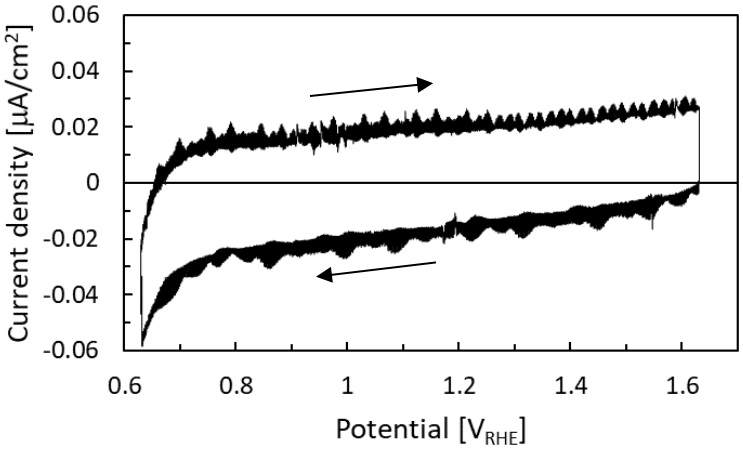

Figure S1. Cyclic voltammogram of the hematite photoanode reported in the article, measured in dark, at a scan rate of 10 mV/s.

S2. Surface charge stored in oxidized intermediates

The cathodic current measured during the entire discharge sequence (starting upon light turn off) was integrated over time to obtain the total charge stored in the oxidized intermediates as a function of the applied potential (U_{high}) in the pre-oxidation (first) stage. This was done for both the modified four-stage CDM presented in the article and for the classical three-stage CDM. The four-stage measurements were performed using fixed initial and final states (U_{high} and U_{low}) while modifying the intermediate (U_{int}) potential values. This set of measurements, represented by pink crosses in Figure S2, was performed to accurately define the baseline for the integration of charge in all sets of measurements. The calibration was performed by linear regression, assuming that the amount of charge stored in the oxidized intermediates depends only on the initial and final conditions, and therefore it is independent of the discharge sequence. The potential value for each cross corresponds to the value of U_{int}. The precise baseline calibration is important for the longer time CDM presented in the article (Figure 3b) where small currents were recorded in the final discharge step, and also to estimate the total amount of charge stored at the oxidized intermediates at low U_{high} potentials in the classical tree-stage CDM.

Three-stage CDM were performed to estimate the total amount of charge stored at oxidized intermediates for different bias potentials (U_{high}) in the pre-oxidation (first) stage. For each measurement the initial potential value U_{high} was modified, as presented by the red dots in Figure S2. The discharge current was integrated starting from the moment the light was turned off. The surface charge is negligible for potentials significantly lower than the photocurrent onset potential, and it increases monotonically with increasing U_{high} values higher than 0.75 V_{RHE}. This result shows that the intermediate states get

oxidized already at potentials lower than the photocurrent onset potential, in agreement with previous studies.[1,2] The surface charge monotonically increases up to the photocurrent plateau region in the LSV scan, where it saturates. This observation suggests that most of the intermediate states are oxidized in the photocurrent plateau region where the current density is limited by the flux of holes arriving from the bulk to the surface.[3] In addition, saturation of the surface charge suggests that if the intermediate states can interact between themselves and transfer the charge when the potential is modified, both of them can hold the same amount of charge.

Assuming a model with two kinds of intermediate states, A and B, the total charge per unit area transmitted in the three-stage CDM would be proportional to $q(\theta_A + \theta_B)$, i.e., proportional to the total surface coverage of both kinds of intermediate states. The total charge scale in Figure S2 was also converted to an average amount of surface holes per iron site on the surface. The conversion was made based on lattice parameters of hematite unit cell,[4] resulting in 8.9 iron sites per 1 nm^2 for (0001) (*c*-plane) terminated surface.

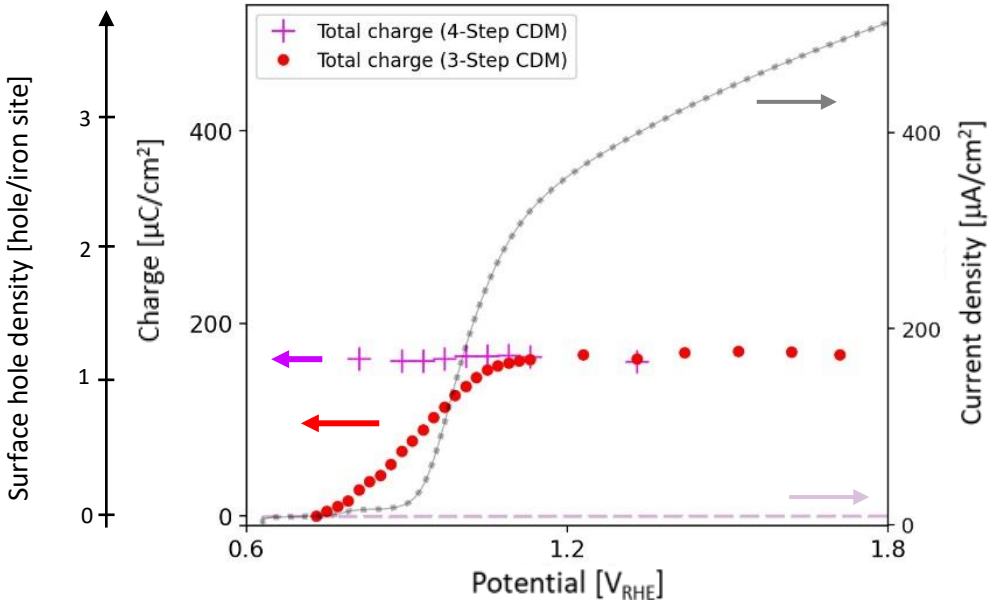

Figure S2. The charge stored in oxidized intermediates as a function of the applied potential (U_{high}) during the pre-oxidation (first) stage in three-stage CDM (red dots), and as a function of the intermediate potential (U_{int}) of the second stage in four-stage CDM with a constant initial potential value of U_{high} = 1.83 V_{RHE} (pink crosses)**.** In both three- and four-stage CDM, the cathodic discharge stage was performed down to a potential of U_{low} = 0.63 V_{RHE} at sweep rate of 200 mV/s. The charge density axis was also converted to an average amount of holes per iron site, as described in the paragraph above. Linear sweep voltammetry curves under illumination (gray dots) and in dark (pale purple dashed line) are overlaid.

S3. Three-step cathodic discharge measurement

Figure S3 presents the results of the classical cathodic discharge measurement (CDM) carried out for the photoanode reported in the article. Here, the CDM has only three stages, instead of the four stages in the modified CDM sequence presented in Figure 3 in the article.

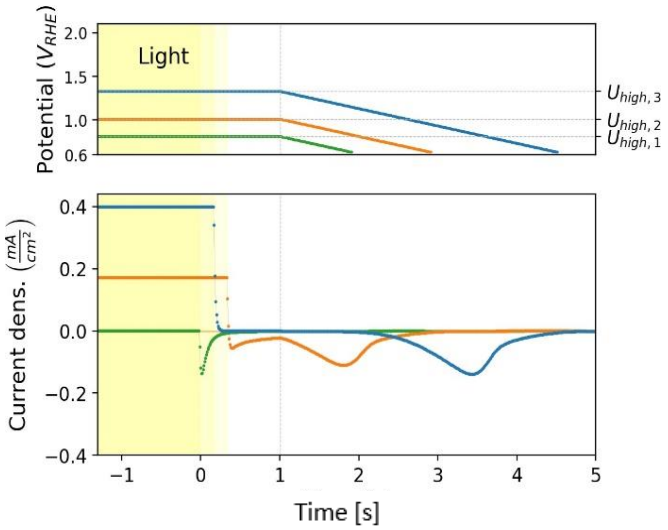

Figure S3. Classical (3 stage) cathodic discharge measurements (CDM) at three different starting potentials (U_{high}) as shown (color coded) on the top panel. The bottom panel shows the current response to changes in illumination and potential in the second and third stages.

S4. Cathodic discharge measurements of different samples

Linear sweep voltammetry and classical three-stage CDM measurements were carried out for the heteroepitaxial Zn-doped hematite photoanode from the article, as well as for additional samples that include hematite doped with different dopants (Sn and Ti) and deposited on different substrates (sapphire, glass and silicon) coated with different current collector layers: Sn-doped indium (ITO), Nb-doped tin (NTO) and platinum. The results for the Zn-doped sample from the article are presented in Figure S4, showing an asymmetric discharge peak for a short delay time (10 s) between turning the light off and sweeping the potential cathodically. This result is in line with the modified 4-step CDM results presented in Figure 3 in the article that demonstrate that longer delay times of over 50 s are necessary to resolve the two peaks, and it further signifies the importance of introducing variable delay times to resolve the two discharge peaks that split out of the asymmetric peak and show up clearly at long delay times. While the samples presented in Figures S5 and S6 display similar results to Figure 3 in the article (double peaks with higher potential peak larger than the lower potential one) even after short delay time between switching off the light and the potential sweep, the discharge peaks presented in Figure S7 are odd due to the presence of steady-state dark current at the potentials in which the cathodic discharge begins.

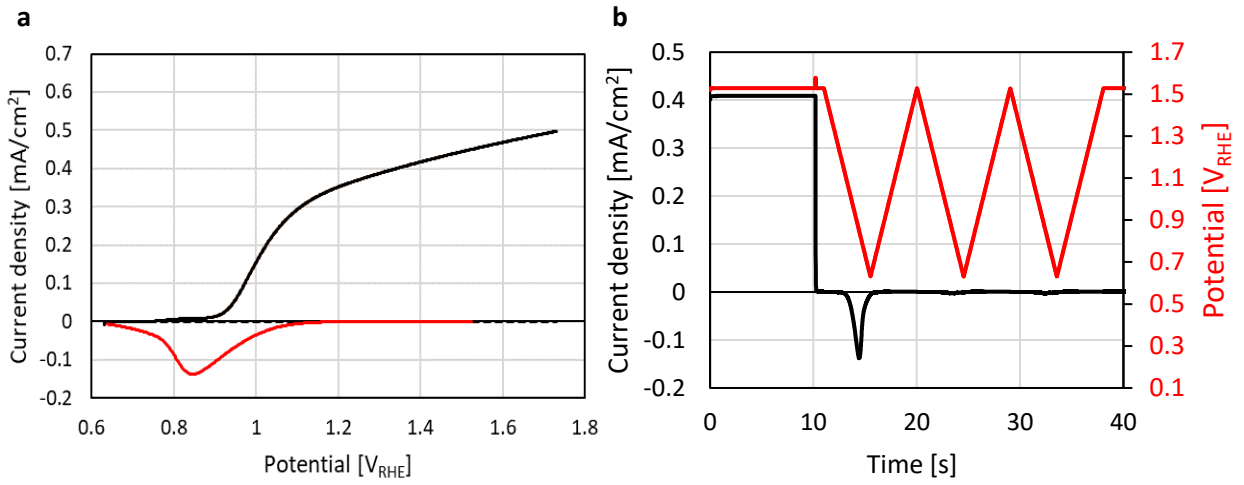

Figure S4. (a) Linear sweep voltammetry (LSV) measurements under dark (black dashed line) and light (black solid line) for a heteroepitaxial 1% (cat.%) Zn-doped hematite film (80 nm thick) deposited by PLD on a lattice-matched Nb-doped (1 cat%) SnO_2 (abbreviated NTO) coated (0001) sapphire substrate. The hematite layer was deposited at 700°C. The cathodic discharge wave observed in Figure S4b is overlaid in red. (b) Three-stage CDM for the same sample.

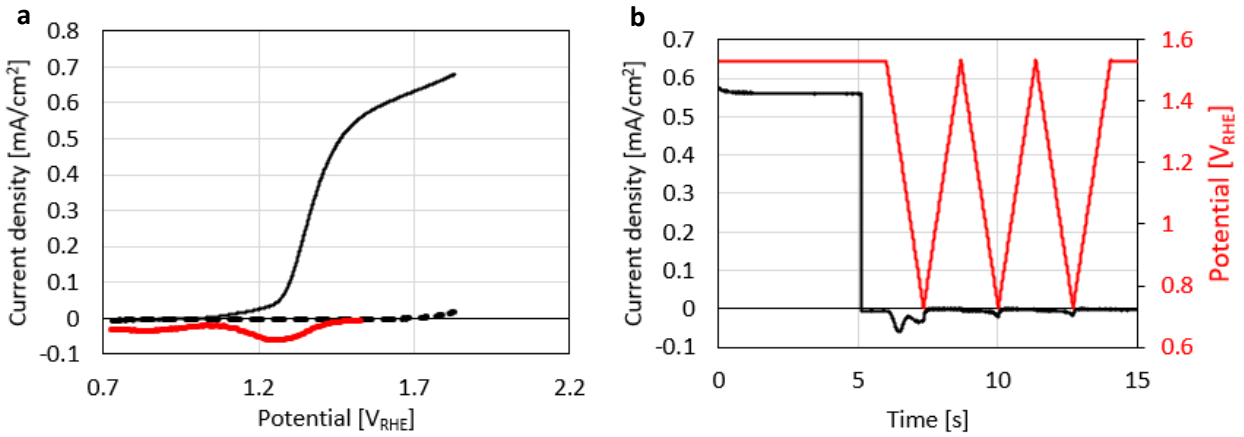

Figure S5. (a) Linear sweep voltammetry (LSV) measurements under dark (black dashed) and light (black solid) for a polycrystalline 1% (cat.%) Sn-doped hematite film (20 nm thick) deposited by PLD on ITO-coated glass substrate (Eagle glass, Corning). The sample was deposited at 300°C and annealed in air for 5 h at 500°C. The cathodic discharge wave observed in Figure S5b is overlaid in red. (b) Three-stage CDM for the same sample.

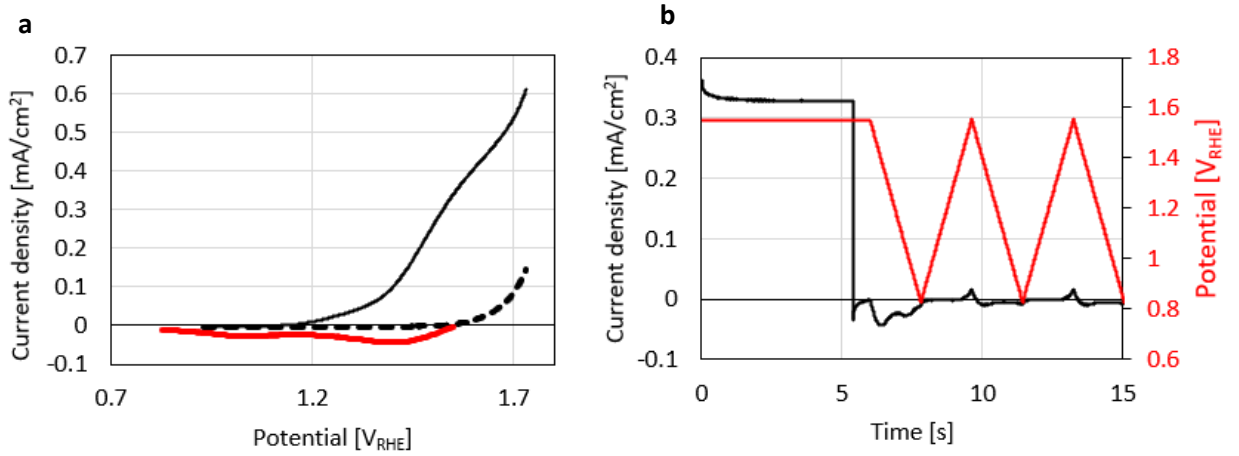

Figure S6. (a) Linear sweep voltammetry (LSV) measurements under dark (black dashed) and light (black solid) for a polycrystalline 1% (cat.%) Sn-doped hematite film (80 nm thick) deposited by PLD on a Si substrate coated with a Pt current collector layer deposited by sputtering. The sample was deposited at 500°C. The cathodic discharge wave observed in Figure S6b is overlaid in red. (b) Three-stage CDM for the same sample.

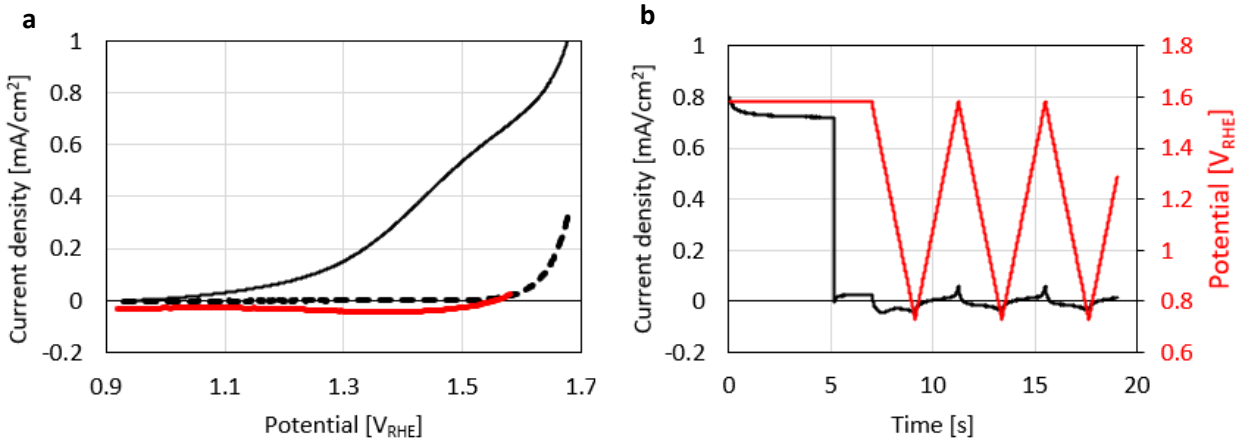

Figure S7. (a) Linear sweep voltammetry (LSV) measurements under dark (black dashed) and light (black solid) for a 1% (cat.%) Ti-doped hematite film (~120 nm thick) deposited by PLD on a TEC15 glass substrate coated with an FTO current collector layer. The sample was deposited at 500°C. The cathodic discharge wave observed in Figure S7b is overlaid in red. (b) Three-stage CDM for the same sample.

S5. Peak reversal

Figure S8 presents delay time dependent CDM for the heteroepitaxial Zn-doped hematite photoanode presented in the article. The measurements was performed in the classical (3-step) sequence, holding the sample at a fixed potential of U_{high} = 1.53 V_{RHE} in the first stage, then the light was turned off in the second stage and the potential was held constant for different delay times (Δt), until finally it was swept to U_{low} = 0.63 V_{RHE} in the third stage (at a sweep rate of 200 mV/s). Complete peak reversal is shown after extended delay times (≥ 100 s, blue curve).

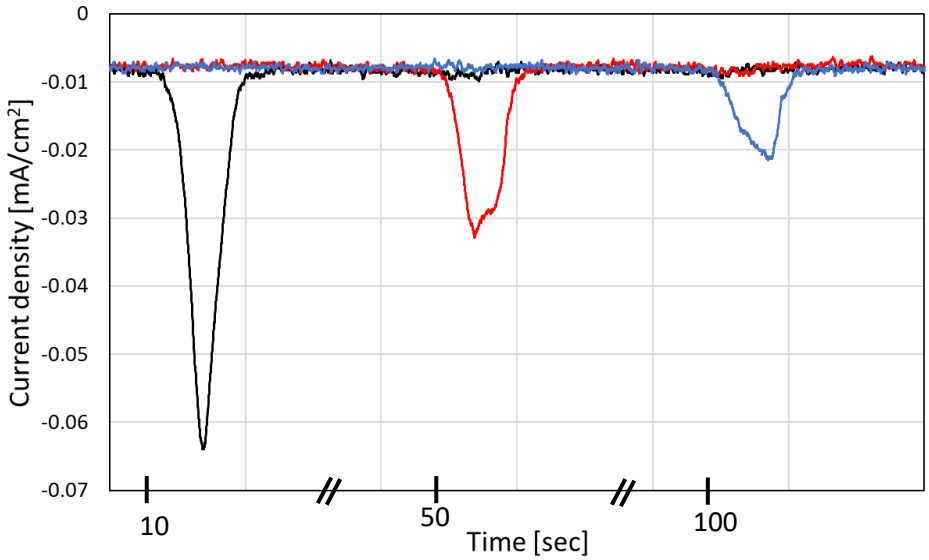

Figure S8. Cathodic discharge waves recorded in the third stage of 3-step CDM with different delay times (Δt) of 10, 50 and 100 s in the second stage (black, red and blue curves, respectively). The sample is the same Zn-doped photoanode reported in the article.

S6. Impedance measurements

Figures S9- to S12 present frequency domain impedance measurements of the photoanode presented in the article, from which the results presented in Figure 4b were extracted. The measurements were taken from 10 kHz to 0.3 Hz at bias potentials ranging from 1.53 to 0.73 V_{RHE} in increments of 0.1 V. Each set of measurements was performed for two light intensities of approximately 0.5 (top panel in each figure) and 1 (bottom panel) sun, using a white-light 4300K LED (LSW-2, Zennium, Zahner Electrik) calibrated to 50 and 100 mW/cm^2 using a Si photodiode. In case of the PEIS measurements presented in Figure S10 the potential was modulated using a 10 mV AC modulation around the baseline DC potential. For IMVS measurements the fixed current was obtained by initially setting the potential to the desired value so as to match the PEIS measurements, and switching to a fixed current after its stabilization under the applied DC potential and light intensity. Then light modulation applied by overlaying a 20 mV AC signal on the DC bias applied of the LED (0.8 or 1.6 V for 0.5 or1 sun light intensities, respectively).

The IMPS results, presented in Figure S11, were calculated by using the following equation: [5]

$$IMPS(\omega) = \frac{IMVS(\omega)}{PEIS(\omega)}.$$

IMPS data fitting

In Figure S12 we show the raw data points (circles) that were used for equivalent cicle fitting in order to extract the forward (hole), backward (recombination) and overall (net) photocurrent, according to the method described in ref. 5. The red lines represent the fitting results. For the three highest potential (1.33, 1.43 and 1.53 V_{RHE}) only one semicircle was fitted due to lack of additional semicircle, as can be observed in the full set of data presented in Figure S11.

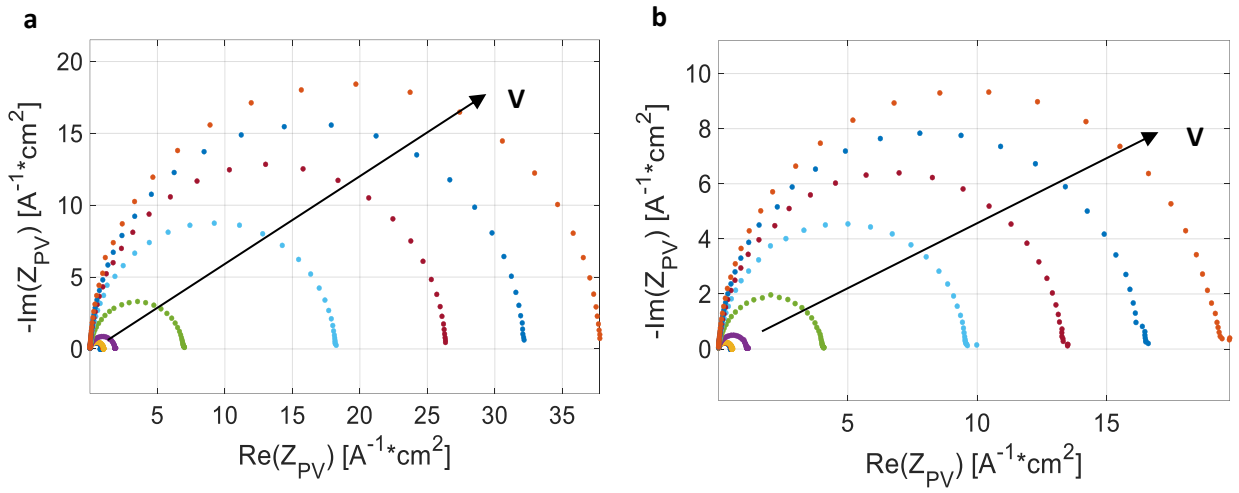

Figure S9. IMVS measurements of the main photoanode reported in the article under white LED illumination of (a) 0.5 and (b) 1 sun. The measurements were performed under a fixed current in the range that corresponds to potential values range of 0.73 – 1.53 V_{RHE} in increments of 0.1 V, as indicated in Figure 4 in the article. The arrow points towards direction of increasing potential.

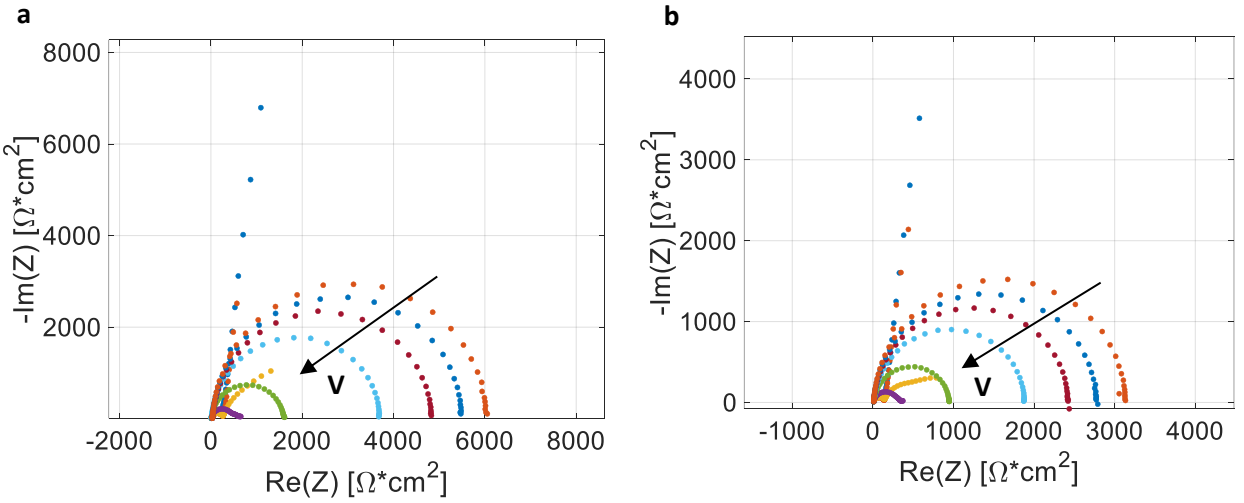

Figure S10. PEIS measurements of the main photoanode reported in the article under white LED illumination of (a) 0.5 and (b) 1 sun. The measurements were performed under a fixed potential values range of 0.73 – 1.53 V_{RHE} in increments of 0.1V, as indicated in a Figure 4 in the article. The arrow points towards direction of increasing potential.

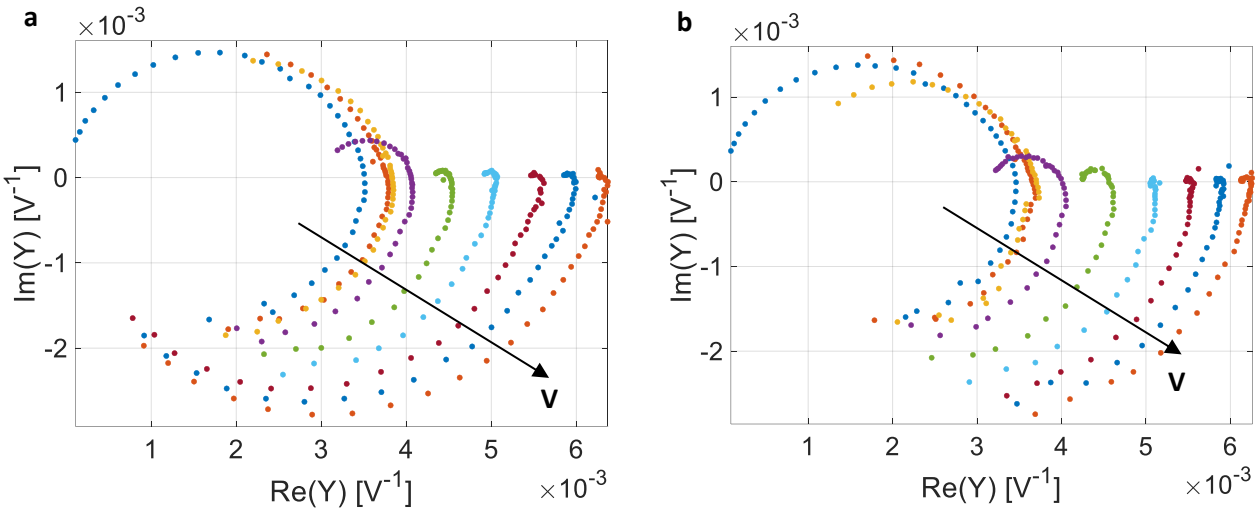

Figure S11. IMPS values calculated from IMVS and PEIS data presented in Figures S9 and S10, respectively.

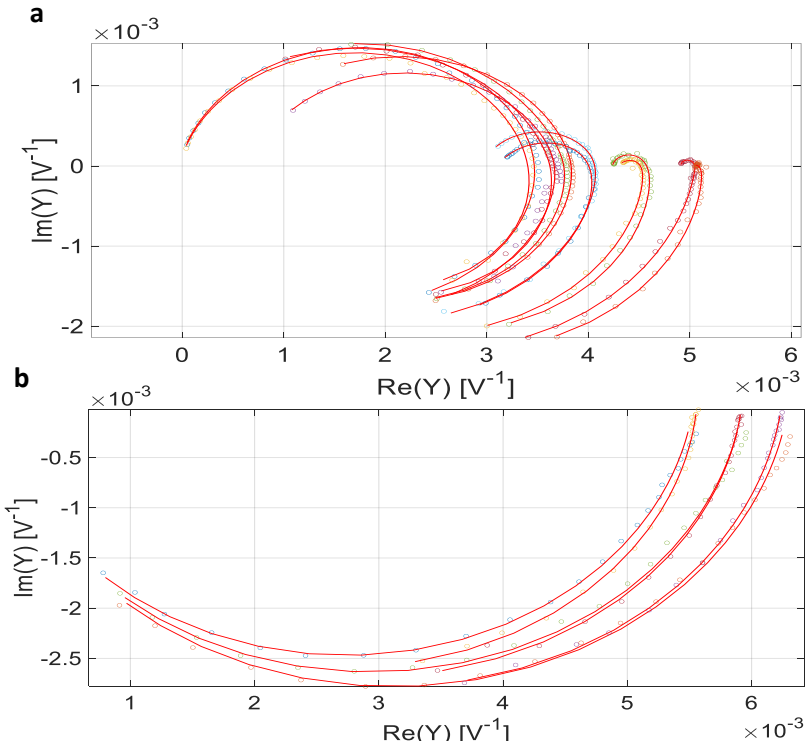

Figure S12. IMPS raw data (open circles) and fitted values (solid red line) for 1% (cat.%) Zn doped hematite sample. The fitted values were used to calculate current density values presented in Figure 5 in the main text, according to method reported elsewhere.[5,6] Panel (a) corresponds to potential values between 0.73 to 1.23 V_{RHE}, for which two semicircles were used to extract both hole bulk and recombination currents. Panel (b) correspond for measurements at potential values of 1.33, 1.43 and 1.53 V_{RHE}, for which only higher frequency semicircle could be fitted to extract hole bulk current values.

S7. Numerical protocol for the modeling of the cathodic discharge measurements

To qualitatively model the experimental protocol of the cathodic discharge measurements reported in the article (see Figure 1b), we set, as a guiding example, the initial values of the surface coverages as $\theta_A^0 = 0.6$, $\theta_B^0 = 0.4$ and $\theta_G^0 = 0$, and solved the model equation for the following potential-time profile:

$$U(t) = \begin{cases} 2, & -250 \le t < 0, \\ U_{int}, & 0 \le t < 500, \\ U_{int} - v(t-500), & 500 \le t < 1250, \\ U_f, & 1250 \le t, \end{cases} \quad \text{(S1)}$$

where U_{int} is a chosen intermediate constant potential and $U_f = U_{int} - 750v$ was set as the final constant potential with $v > 0$. We solve equations (4)-(6) for each time interval and impose continuity. The resulting current densities for sequential and parallel pathways are shown Figure S13. We demonstrate the qualitative consistency with the experimental results (see Figure 1b), especially the shift in the peak maximum in the parallel pathway, by using three values of U_{int}.

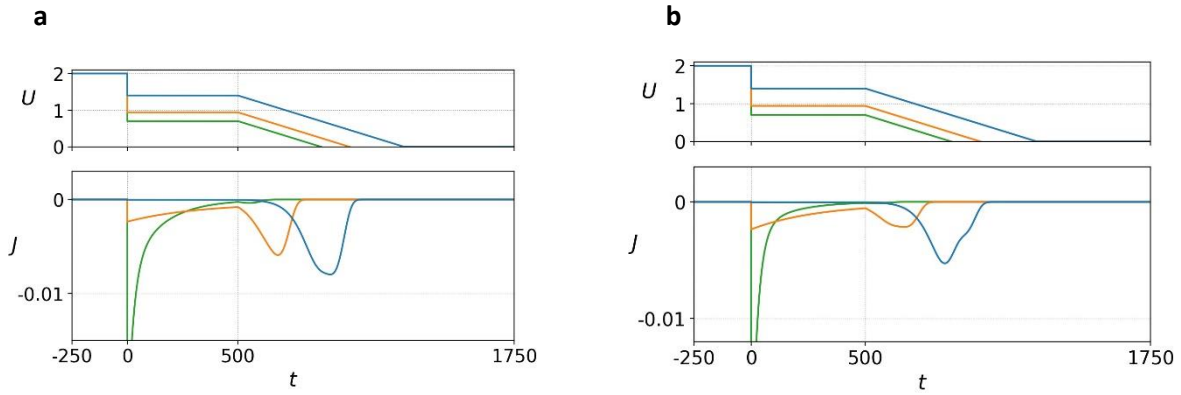

Figure S13. Current densities that are computed according (7) for the sequential reaction pathway (a) and for the parallel reaction pathway (b) upon applied potentials (S1), with $U_{int} = 1.4$ (blue), $U_{int} = 0.94$ (yellow), $U_{int} = 0.7$ (green) and $v = 0.0018$. Other parameters: $\theta_A^0 = 0.6$, $\theta_B^0 = 0.4$, $\beta = 10$, $\gamma = 1$, $k_A = 42.5$, $k_B = 7.5$.

S8. Qualitative difference between the sequential and the parallel pathways: reversal of the peaks

To uncover the qualitative properties of the sequential and parallel pathways we focus on the linear sweep interval of the applied potential, $U(t) = U_0 - v(t - t_0)$, see equation (S1). Following equation (7) the current density $J_A(t)$ is a product of two counter monotonic behaviors with time: a decreasing function $e^{-k_A\Phi(t)}$ and an increasing function $e^{-\beta U(t)}$. Hence, the product of both may emerge in a peak-shape current density, see current densities indicated by blue line in Figure S14. For analysis purposes, we seek for peak-shape solutions, i.e., where the derivative of $J_A(t)$ is continuous and with a single change of sign at some unique point t_A^*, and which also satisfy $J_A^0 \equiv J_A(t_0) \ll J_A^*$, where $J_A^* \equiv J_A(t_A^*)$. From equation (4) we obtain that $t_A^* = -(v\beta)^{-1}\ln(k_A Z) + t_0$, where $Z \equiv (\gamma/v\beta)e^{\beta U_0}$, and since $t_A^* \ge t_0$ must naturally hold, we get $k_A Z \le 1$ and thus, along with $J_A^0/J_A^* = k_A Z \cdot e^{(1-k_A Z)} \ll 1$, we deduce the necessary and sufficient condition: $k_A Z \ll 1$. Similarly, $J_{B,par}(t)$ has a peak-shape solution with $t_{B,par}^* = -(v\beta)^{-1}\ln(k_B Z) + t_0$ if and only if $k_B Z \ll 1$, where $t_{B,par}^* > t_A^*$ since $k_A > k_B$. Analysis of

$J_{B,seq}(t)$, however, shows that $t^*_{B,seq}$ has no closed analytic form and therefore, computed numerically. In Figure S14, we illustrate these quantities, together with the resulting total current density, while in Figure S15, we demonstrate how the location of the peak solution shifts upon several scan-rates. We emphasize that the analytic form of $J_A(t)$ indicates that if it has a peak-shape solution (for $k_A Z \ll 1$) then $J_{B,seq}(t)$ also has a global maximum point $t^*_{B,seq}$, with maximum value $J^*_{B,seq} \equiv J_{B,seq}\left(t^*_{B,seq}\right)$ such that $t^*_{B,seq} > t^*_A$. The latter follows from two propositions: (i) $k_A Z \ll 1$ and $k_A > k_B$ implies that the derivative $\dot{J}_{B,seq}(t)$ is strictly positive in the interval $[t_0, t^*_A]$, (ii) since $J_{B,seq}(t) \geq 0$, $\lim_{t\to\infty} J_{B,seq}(t) = 0$ and the integral of $J_{B,seq}(t)$ from t_0 to t_∞ is bounded, then the global maximum $t^*_{B,seq}$ exists vis $t^*_{B,seq} > t^*_A$, although the value of $t^*_{B,seq}$ remains unknown.

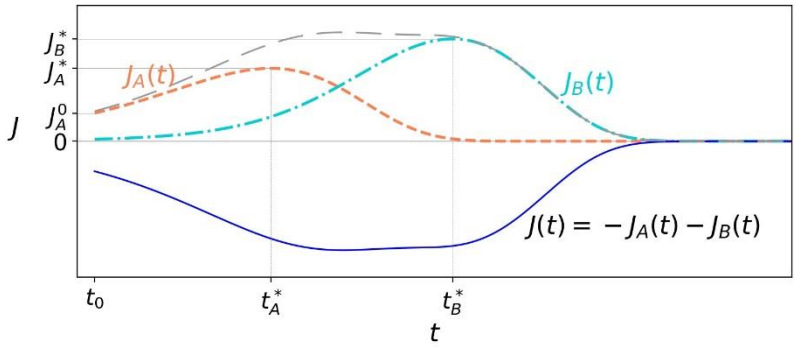

Figure S14. Representation of the total current density $J(t)$ by superposition of two partial contributions of the current $J_A(t)$ and $J_B(t)$, see text for details.

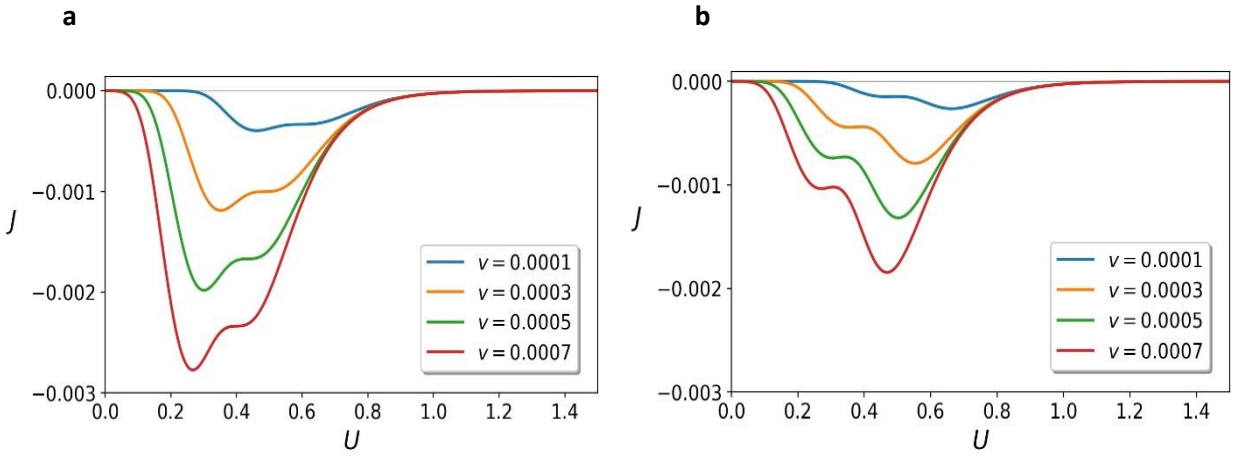

Figure S15. Selected current densities upon linear potential sweep from $U = U_0$ to $U = 0$ and scan rates v, showing the peak-shape variation for the sequential (a) and the parallel (b) pathways. Parameters: $U_0 = 1.5$. $\theta^0_A = 0.6$, $\theta^0_B = 0.4$, $\beta = 10$, $\gamma = 1$, $k_A = 0.9$ and $k_B = 0.1$.

The obtained above properties allow us to uncover the inherited qualitative difference associated with peak reversals, as discussed in the main text. From (4), (6) and (7) and assuming that $J_A(t)$ has a peak-shape, the ratio of heights for the parallel pathway in terms of initial surface coverages is:

$$\frac{J_A^*}{J_{B,par}^*} = \frac{\theta_A^0}{\theta_B^0} e^{(k_A - k_B)Z} \approx \frac{\theta_A^0}{\theta_B^0}. \quad \text{(S2)}$$

For the sequential pathways we cannot obtain analytical approximations as for the parallel pathway, yet we can exploit some of the properties and reach a critical information about the height ratio. If the global maximum $J_{B,seq}^*$ exists, then by definition, any point t satisfies $J_{B,seq}(t) \le J_{B,seq}^*$ and evaluation of $J_{B,seq}(t)$ at the known value $t_{B,par}^*$, yields $y_{B,seq} \equiv J_{B,seq}(t_{B,par}^*) \le J_{B,seq}^*$. Thus, if $J_A(t)$ has a peak-shape solution, which implies that $J_{B,seq}^*$ exists, we can exploit the approximation $y_{B,seq} \approx J_{B,par}^* + J_A^* \cdot f(\lambda)$, where $\lambda = k_B/k_A < 1$ and $f(\lambda) = \left[1 - e^{-(1-\lambda)/\lambda}\right]/(1-\lambda) \ge 1$. The approximation can be verified by the evaluation of the function $J_{B,seq}(t)$ at $t_{B,par}^* = -(\nu\beta)^{-1}\ln(k_B Z) + t_0$, requiring that $k_B Z < k_A Z \ll 1$. Therefore,

$$\frac{J_A^*}{J_{B,seq}^*} \le \frac{J_A^*}{y_B} \approx \frac{J_A^*}{J_{B,par}^* + J_A^* \cdot f(\lambda)} = \frac{1}{f(\lambda) + J_{B,par}^*/J_A^*} \le 1. \quad \text{(S3)}$$

This indicates that for a sequential pathway, the height of the peak $J_A(t)$ will always be lower than the maximum value of $J_{B,seq}(t)$, independent of the $J_{B,seq}(t)$ shape, namely precluding peak height reversal. Indeed, experimental measurements in Figure 3, show that J_A^* can be few times bigger than $J_{B,seq}^*$, which discards the sequential pathway as the underlying mechanism.

For validation of (S2) and (S3), we solve numerically the kinetic model equations that satisfy $k_A Z, k_B Z \ll 1$ and employ the limits $\lambda = 1$ $(k_A = k_B)$ and $\lambda = 0.01$ $(k_A \gg k_B)$, as shown in Figure S16. Those limits were chosen to verify consistency with experimental results in Figure 3d showing monotonic variation about two orders of magnitude in the current density. Importantly, we also found that the results largely hold for $k_A Z \sim 0.1$ (not shown here).

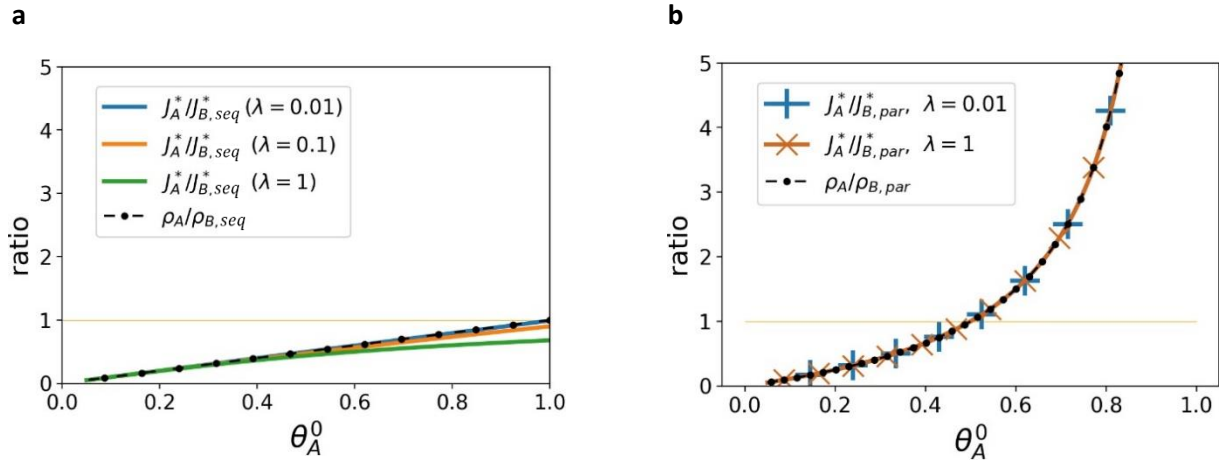

Figure S16. Numerically computed ratio J_A^*/J_B^* (solid colored lines) for (a) sequential pathway and (b) parallel pathways, for several $\lambda \equiv k_B/k_A$ values and with $k_A + k_B = 50$. $\theta_B^0 = 1 - \theta_A^0$, $\beta = 10$, $\gamma = 1$, $U_0 = 2$, $\nu = 0.0018$. The analytical approximations are superimposed (black line), showing $\rho_A/\rho_{B,seq} = \theta_A^0/(\theta_A^0 + \theta_B^0)$ and $\rho_A/\rho_{B,par} = \theta_A^0/\theta_B^0$, respectively.

REFERENCES

1 L. M. Peter, *J. Solid State Electrochem.*, 2013, **17**, 315–326.

2 B. Klahr, S. Gimenez, F. Fabregat-Santiago, J. Bisquert and T. W. Hamann, *Energy Environ. Sci.*, 2012, **5**, 7626.

3 H. Dotan, K. Sivula, M. Grätzel, A. Rothschild, S. C. Warren, J. Tucek, J. Frydrych and M. Grätzel, *Energy Environ. Sci.*, 2011, **4**, 958–964.

4 R. M. Cornell and U. Schwertmann, *The iron oxides : structure, properties, reactions, occurrences, and uses.* Vol. 2. Wiley-VCH, Weinheim, 2003.

5 D. Klotz, D. S. Ellis, H. Dotan and A. Rothschild, *Phys. Chem. Chem. Phys.*, 2016, **18**, 23438–23457.

6 D. Klotz, D. A. Grave and A. Rothschild, *Phys. Chem. Chem. Phys.*, 2017, **19**, 20383–20392.